Tectonic Geomorphology and Paleoseismology of the Sharkhai fault: a new source of seismic hazard for Ulaanbaatar (Mongolia)

Abeer Al-Ashkar[1], Antoine Schlupp[1], Matthieu Ferry[2], Ulziibat Munkhuu[3]

5 [1]Institut Terre et Environnement de Strasbourg, UMR 7063, Université de Strasbourg/EOST, CNRS ; 5 rue René Descartes, Strasbourg, 67084, France

[2] Géosciences Montpellier, Université de Montpellier - CNRS, Montpellier, France

[3] Institute of Astronomy and Geophysics, Mongolian Academy of Sciences, Ulaanbaatar, Mongolia

Correspondence to: *Antoine Schlupp (antoine.schlupp@unistra.fr)*

Abstract. We present new constraints from tectonic geomorphology and paleoseismology along the newly discovered Sharkhai fault near the capital city of Mongolia. Detailed observations from high resolution Pleiades satellite images and field investigations allowed us to map the fault in detail, describe its geometry and
15 segmentation, characterize its kinematics, and document its recent activity and seismic behavior (cumulative displacements and paleoseismicity). The Sharkhai fault displays a surface length of ~ 40 km with a slightly arcuate geometry, and a strike ranging from N42°E to N72°E. It affects numerous drainages that show left-lateral cumulative displacements reaching 57 m. Paleoseismic investigations document the faulting and deposition record for the last ~ 3000 yr and reveal that the penultimate earthquake (PE) occurred between 1515 ± 90 BC and 945 ±
20 110 BC and the most recent event (MRE) occurred after 860 ± 85 AD. The resulting time interval of 2080 ± 470 years is the first constraint on the Sharkhai fault for large earthquakes. On the basis of our mapping of the surface rupture and the resulting segmentation analysis, we propose two possible scenarios for large earthquakes with likely magnitudes between 6.4 ± 0.2 and 7.1 ± 0.2. Furthermore, we apply scaling laws to infer coseismic slip values and derive preliminary estimates of long-term slip rates between 0.2 ± 0.2 and 1.0 ± 0.5 mm/y. Finally, we
25 propose that these original observations and results from a newly discovered fault should be taken into account for the seismic hazard assessment for the city of Ulaanbaatar and help build a comprehensive model of active faults in that region.

Introduction and context

30 The tectonics of Mongolia are characterized by a transition region between the compressive structures associated with the India-Asia collision to the south and the vast extensive structures of the Baikal Rift to the north (Fig. 1). This induces numerous strike-slip structures and uplift in west and central Mongolia with minor thrust and normal faults (Khilko et al., 1985; Cunningham, 2001; Ritz et al., 2003; Cunningham, 2007; Walker et al., 2008; Parfeevets and Sankov, 2012). In Central Mongolia, the Hangay dome displays several regional SW-NE extensive structures
35 and is surrounded by right- and left-lateral faults (Cuningham et al., 1996; Schlupp, 1996; Bayasgalan, 1999;

Bayasgalan et al., 1999a, Etchebes, 2011). Western Mongolia is dominated by NW-SE-striking right-lateral and thrust faults distributed across the Mongolian Altai ranges, while southern Mongolia shows E-W left-lateral and thrust faults that produce the Gobi Altay restraining-bend topography. Finally, to the north the E-W Bolnay left-lateral strike-slip fault begins the transition with the Baikal rift system. Presently, the knowledge of historical

40 seismicity in the region is poorly constrained (Khilko et al., 1985). Since 1905, the seismicity has been highlighted by four great earthquakes of Mw > 8 (9 and 23 July 1905, 11 August 1931 and 4 December 1957) which occurred along the strike-slip faults of western Mongolia (Fig. 1) and moderate background activity. The observed rate of deformation along the faults, in western and central Mongolia, are relatively low with 1.5 ± 0.26 to 3.8 ± 0.2 mm/yr based on geological observations (Ritz et al., 2006; Etchebes, 2011; Rizza et al., 2015) and 2 ± 1.2 to 2.6 ± 0.5

45 mm/yr based on geodetic data (Calais et al., 2003).

The situation differs around the capital Ulaanbaatar where the recorded seismicity is much lower. The historical seismicity is poorly known and since 1957, when the instrumental period started, the activity has been limited to moderate earthquakes with magnitude less than 4.5 (Adiya, 2016). Nevertheless, several earthquakes were largely felt in Ulaanbaatar during the last century (Intensity MSK up to VI) without significant damage. Regional

50 deformation characterized by geodesy indicates 2-4 mm/yr of E-SE horizontal displacement with respect to Eurasia with the main part absorbed by the Baikal rift system (Miroshnichenko et al., 2018).

Since 2005, a stronger seismic activity (M ≤ 4.5) has been observed ~ 10 km west of the capital, around the newly discovered Emeelt fault (Schlupp et al., 2010a), which prompted studies in tectonic geomorphology and paleoseismology to characterize some of the few known active faults (Hustai, Gunj, Emeelt) and extend the

55 catalogue of potential seismic sources (see below for references)..

Hustai (Khustai) fault: Located ~ 30 km west from Ulaanbaatar, the fault exhibits a striking morphology but has been studied only recently. It is a left-lateral fault with a normal component, composed of several segments with a total length of 212 km and able to produce earthquakes of M 6.5-7.5 (Ferry et al., 2010; Schlupp et al., 2010b; Fleury et al., 2011; Ferry et al., 2012).

60 Gunj fault: Located ~ 15 km north-east from Ulaanbaatar, it has a length of ~ 20 km and is oriented N45°. It is associated with right-lateral displacement, vertical component and flower structures (Imaev et al., 2012).

Emeelt fault: This fault has also been identified recently using tectonic geomorphology following a seismic swarm that started in 2005 and concentrated within a small area ~ 10 km west of Ulaanbaatar. Between 2005 and 2019, more than ten swarm episodes of moderate earthquakes M ≤ 4.5 have been recorded (Adiya, 2016). The Emeelt

65 fault, located near the eastern end of the Hustai fault, strikes N140° (Fig. 2) and displays dominantly right-lateral kinematics with a reverse component. Recent studies suggest that it could produce earthquakes of magnitude 6-7 (Ferry et al, 2010; Schlupp et al, 2010a; Ferry et al, 2012; Schlupp et al., 2012; Dujardin et al, 2014).

The Ulaanbaatar region is situated in a folded system composed of Lower Carboniferous (C1 Altan-Ovoo formation), Lower-Middle Carboniferous (C1-C2 Orgioch-Uul Formation) and Quaternary deposits (Tomurtogoo

70 et al, 1998, Manandhar et al., 2016) (Fig. 3). The Altan-Ovoo and Orgioch-Uul formations are sandstone, mudstone, alternating beds of sandstone and mudstone with small amounts of conglomerate, siliceous mudstone, chert, felsic tuff and basalt (Takeuchi et al., 2013). In addition, Ulaanbaatar is located at the Tuul River Valley on

a sedimentary basin of alluvial deposits with a maximum thickness of about 120 m that induces site effects which amplify the ground motion during earthquakes (Odonbaatar 2011, Tumurbaatar et al., 2019). Although the geological map (Fig. 3) displays several tectonic faults distributed in the Ulaanbaatar area their potential Quaternary activation is unknown.

Ulaanbaatar is the commercial and industrial center of Mongolia with a concentration of nearly half of the country's population (about 1.5 million in the capital of 3.2 million, according to the national statistics office of Mongolia, 2018). The growth of the capital is very important since the last two decades, the population in 1998 being lower than 0.7 million. In terms of seismic risk, the population is spread in buildings with various vulnerability qualities. The masonry structures are major (62%) in Ulaanbaatar, steel structures (18%), wooden structures and Gers (2%). Masonry buildings (usually apartments) are considered seismically safe, but the first floor is modified inconsiderately to transform them to shops or restaurants, making the building weaker for seismic resistance (Dorjpalam et al., 2004). The stakes and their location are also modified. For example, in the city, new tall buildings have been erected and at 30 kilometers to the south a new international airport has been constructed, that should be operational in 2021, replacing the actual too short and now too close to the urbanised city.

The discovery of potential active faults and the development of the capital and its infrastructures suggests us to search for other unknown active structures that could exist around the capital. Our studies concern only the faults for which there were signs of Quaternary seismic activity. We investigated the southern area close to the new international airport. Using high resolution satellite images and field investigations, we discovered surface traces of two active faults we call "Sharkhai fault" and "Avdar fault", which shows clear evidence for a major seismic activity (Fig. 2) (Al-Ashkar, 2015).

Here, we present the Sharkhai fault located ~ 35 km south of the capital and only 10 km south of the new airport. Along the Sharkhai fault, few moderate earthquakes (M ≤ 3.7) were observed between 2004 and 2007. We present hereafter evidence of holocene activity, based on remote sensing analysis, geomorphological observations and paleoseismological investigations, and associated characteristics (detailed mapping, kinematic, identification and dating of past earthquakes, recurrence time of large events).

1 Morphotectonic description

1.1 Surface trace Mapping

1.1.1 Methodology

Considering the combined very well-expressed geology, and low deformation, erosion and sedimentation rates, our strategy consisted in mapping background faults at high spatial resolution and characterizing their subtle expression within Quaternary deposits. We based our analysis on very high resolution orthorectified Pleiades satellites images (multispectral RGB-NIR at 2 m resolution and panchromatic at 0.5 m resolution) and high-resolution digital elevation models (hereafter DEM; SRTM 1" at 30 m resolution and TanDEM-X at 12 m resolution) to identify and quantify horizontal and vertical deformation. In addition, we used Google Earth images for specific areas where multi-date data could complement Pleiades images. Remote sensing analysis was

supplemented by field campaigns to verify, correct and complement our observations, perform detailed geomorphological mapping and excavate a paleoseismological trench.

1.1.2 Overview

Our observations show that the main trace of the Sharkhai fault, striking ENE-WSW, extends along 40 km (from A1 to A7 in Fig. 4). It is associated with eroded and smoothed surficial ruptures that die off beyond the end points. We did not observe any connection with other known active structures. The Sharkhai fault does not follow any obvious geological feature or limit documented by the national geological map (Tomurtogoo et al., 1998).

The most obvious characteristic is the presence of an extensional jog of 1.4 km width associated with a 13° clockwise change of the main fault strike (Fig. 4, A3 and A4). It suggests that the Sharkhai fault can be subdivided into two major sections: the south section (strike N42 to N55) and the north section (strike N55 to N72) (Fig. 4). We observe in the field only an apparent vertical offset (about 30 cm) along the north section near the trench site (see details in the paleoseismology section).

We describe hereunder the surface traces from the southwest to the northeast and detail the various features documenting recent activity.

1.1.3 Southern section

The south section runs for ~ 22 km between points A1 and A3 (Fig. 4) where the fault trace dies out at the large extensional step-over. On satellite images and in the field, we can follow the surface traces, despite their weak geomorphologic expression, except some places where they cannot be observed due to erosion or recent deposition from local streams. The main geometric features that we detail here are strike changes and step-overs.

At its southern extremity, between locations A1 and A2 (Fig. 4) the fault strikes N42°E on average. There, from south to north, we observe several small step-overs with size between 3, 7 and 70 m width. The average direction of surface traces, at A2, turns from about N42°E to N50°E, which is the largest strike variation along the south section. From A2, the surface traces cut a Carboniferous hill (1450 to 1645 m elevation). We observe locally several changes in strike over short distances.

Between A2 and B, the fault cuts the top of two successive hills that are oriented N5° and N330°, where drainage P1 recorded 57 ± 2 m of cumulated left-lateral offset (Fig. 4, P1 and Fig. 5). It corresponds to the maximum offset identified along the Sharkhai fault (Table 1). The minimum offset observed (Fig. 4, P2) is 6.25 ± 0.65 m left-lateral strike slip (Fig. 6). Four other left-lateral cumulative offsets are identified and measured at P3 = 36 ± 4 m (Fig. 7), P4 = 30 ± 3 m (Fig. 8), P5 = 6.5 ± 0.5 m (Fig. 9) and P6 = 36 ± 1 m (Fig. 10).

Between B and A3 (Fig. 4), the average strike of the fault is N47°. The fault is arranged in echelons between B and C (Fig. 11). Several secondary branches are observed parallel or oblique to the fault trace. Their lengths range between 190 m and 1.6 km and strike between N 58° E and N 74° E. Beyond, the fault continues through a valley with Quaternary alluvial deposits where we lost locally its trace.

1.1.4 Northern section

The north section runs for ~ 22 km from point A4 (Fig. 4, A4) to point A7 (Fig. 4, A7) affecting mostly Quaternary
145 surface deposits. Its trace runs into an area of lower elevation (mainly < 1500 m) than the south section (mainly >
1500 m). In many places, we lost the fault trace when it crosses wide Quaternary deposits, which could suggest
limited recent surface deformation. The drainage pattern along the north section is less complex but also less
frequent or preserved, limiting possible records of displacement. The north section has slightly arched shape
geometry, its strike turns from N 55° E to N 63° E and N 72° E. At the northern part of the section, we measured
150 57 ± 1 m of left lateral horizontal slip on a stream (Fig. 4, P7 and Fig. 12), the only one identified along the north
Sharkhai section. In contrast to the south section, it shows no step-overs. However, there are more secondary
branches bordering the north fault section, sub-parallel or oblique. Their length is between ten meters and a few
kilometers. We also observe locally several changes in main fault strike over short distances that are presented in
Fig. 13 (insert 2 and 3).

155 As it reaches the SE part of the Khoshigt Khondii basin where the new international airport of Ulaanbaatar is built
(point A7 in Fig. 4), the trace of the Sharkhai fault cannot be observed anymore within Quaternary sediments,
neither on remote sensing data nor in the field.

160 **Table 1: Summary of cumulative left lateral offsets measured on the Sharkhai fault.**

Drainage name	P1	P2	P3	P4	P5	P6	P7
Horizontal offset (m)	57 ± 2	6.25 ± 0.65	36 ± 4	30 ± 3	6.5 ± 0.5	36 ± 1	57 ± 1

2 Fault segmentation

Possible rupture scenarios and associated magnitudes along the Sharkhai fault are key parameters for estimating
165 seismic hazard levels onto the city of Ulaanbaatar and the new airport. Without information about the historical
seismicity along the fault, we may estimate the magnitude of possible events in relation to the length of the rupture
(Wells and Coppersmith, 1994). We use the identified discontinuities along the fault to discuss whether the fault
should be divided into several segments that could break independently or not.

Step-overs, secondary branches, and fault strike changes can play an important role in the propagation of a rupture
170 (nucleation and barrier) and consequently in the size of expected earthquakes (Poliakov et al., 2002; Wesnousky,
2006; Klinger, 2010; Finzi and Langer, 2012; Biasi and Wesnousky, 2016 ; Biasi and Wesnousky, 2017). Usually,
only kilometer-scale discontinuities are taken into account for the segmentation (Crone and Hailer, 1991; De Polo
et al., 1991; Harris et al., 1991, Wesnousky, 2006). Therefore, only the central step-over appears wide enough to
separate the fault into two segments, south and north. The width of the other step-overs are much more limited,

175 between three and 173 m, and are not clearly expressed in the geomorphology. Thus, we do not consider them as segment boundaries.

Similarly, it has been proposed that changes in strike of more than 5° could play a role in fault segmentation (Lettis et al., 2002; Harris et al., 1991, Wesnousky, 2006; Finzi and Langer, 2012), but recent large earthquakes in Mongolia have shown that even larger changes in orientation had no impact for the segmentation [Mogod 1967

180 January 5 Mw 7.1 (Bayasgalan and Jackson, 1999b); Bogd 1957 December 4 Mw 8 (Rizza et al., 2011)]. Along the Sharkhai fault, the changes in the orientation are either very local variation or of value not exceeding 9°. Thus, they are not considered as likely segment boundaries.

In conclusion, we propose two possible scenarios for large earthquakes on the Sharkhai fault (Fig. 13) depending on the role that the central step-over may play in the propagation of the rupture. The first scenario is that the entire

185 fault (40 km) breaks during one earthquake. The second scenario is that the south segment and the north segment (22 km each) break independently.

3 Paleoseismic Investigations

To retrieve the chronology of surface-rupturing paleoearthquakes, we conducted the first paleoseismological study

190 along the Sharkhai Fault at a site called Muka (Fig. 4 and 14). This site was selected based on geomorphological observations performed from high-resolution Pleiades satellite images, high-resolution TanDEM-X DEM and field surveys. Considering a priori slow rate of deformation, our strategy was to avoid apparently recent deposits found in wide alluvial valleys (as well as associated erosion processes) and rather target relatively slow deposition processes such as colluvium on gentle slopes and abandoned or intermittent drainages. The subtle

195 geomorphological expression of the Sharkhai fault combined with high topography along most of its trace yielded only a few favorable sites where the fault is well expressed and potentially datable deposits are expected. The Muka site is located near the Zuunmod - Buren Road and ~ 10 km SW of the new airport. There, the trace of the fault is clear, enhanced by a small scarp (< 50 cm high) (Fig. 14 c), which suggests apparent vertical deformation, and a striking difference in vegetation type and color, often indicative of a local contrast in lithology and/or

200 hydrology in the shallow sub-surface. The fault affects surface colluvium deposited along the flank of a small valley. Local gullies are intermittent and probably only active during important rainfall. Hence, we consider this site favorable to the accumulation of deposits suitable to preserve the fault's paleoseismic history and help determine its timing by radiocarbon and/or OSL approaches.

The Muka site is located along a straight section of the fault where deformation at the surface appears well localized

205 (Fig. 14). There, the fault marks a break in slope and is crossed by short (100-500 m in length) shallow gullies. We excavated two trenches called Muka-K and Muka-L (Fig. 14 b) ~150 m apart. Both trenches were ~20 m long, 1 m wide and up to 3 m deep as limited by the local permafrost. Heavy rainfall and thawing of the exposed permafrost destabilized fine deposits (silt and sand) found in Muka-K overnight. Wide sections of the trench collapsed and the exposure was considered unsafe to work on. Stable substratum crops out at the bottom of Muka-

210 L, which stabilized the whole section and gave time to reinforce with wooden shores. Here, we present and discuss the Muka-L exposure.

3.1 Trench Stratigraphy

215 Both trench walls were cleaned, photographed, gridded and logged in detail. The Photomosaic of the trench (west and east wall) is 15 m long and 3m deep, it is constructed using 210 photographs. Since the both walls yield similar information in terms of paleoseismicity, we only present the west wall in detail along with close-ups of the east wall for illustration (Fig. 15). In the following, we describe the stratigraphy, provide age constraints on the basis of radiocarbon-dated sediment samples and analyse abutting relationships to decipher the chronology of surface-rupturing earthquakes at this site.

220 The base unit visible along the whole trench is composed of massive Carboniferous bedrock (U70) that exhibits widespread fracturation, localized shear zones with thin gouge development (< 2 cm). The uppermost 10-50 cm of U70 are composed of deeply weathered, well-sorted unstratified fine clasts (< 3 cm) that we interpret as the product of gelifraction. Numerous thin shear zones marked by whitish-to-yellowish clay cut through the whole unit and stop at its top surface. They generally exhibit a relatively steep dip to the south and produce duplexing

225 features within the weathered part of U70. The top surface is very rough with deep troughs and systematically truncates reverse-geometry shear zones; it is interpreted as a well-developed erosion surface.

Over the northern section of the trench, U70 is overlain with a ~1-m-thick unit of massive clast-supported coarse gravels and pebbles (U60). Clasts present the same lithology as U70, are very angular and well-stratified, which suggests they have been transported by water over a very short distance. Combining with the geometry of the

230 lower erosion surface, we interpret U60 as a channel fill. U60 contains a few lenses of dark brown to black fine sand. Sample W3-S03 (Fig. 15g and Table 2) was collected within such a lens and yields a radiocarbon age of 3220 ± 30 yr BP calibrated to 1515 ± 90 BC.

Table 2: Radiocarbon dating of sediment samples collected from the Muka-L trench. The software OxCal V2.4 (Ramsey, 2013) with 2 sigma error was used to obtain the calendric ages with Intcal13 calibration curve (Reimer et al., 2013.

Sample name	Stratigraphic unit	Radiocarbon age (yr BP)	Calibrated date (2-sigma)
Muka-L-W2-S06	U11 (mid-section)	1180 ± 25	860 ± 85 AD
Muka-L-W4-S02	U11 (base)	2360 ± 30	450 ± 70 BC
Muka-L-W2-S05	U20	1950 ± 30	45 ± 80 AD
Muka-L-W3-S04	U20	2745 ± 30	945 ± 110 BC
Muka-L-W3-S03	U60	3220 ± 30	1515 ± 90 BC

235 Over the southern section of the trench, U70 is overlain by a ~8-m-wide, 50-cm-thick unit that pinches out at both tips (U50). This latter unit contains similar clasts (in nature and size) to what is observed in U60 with a much smaller matrix fraction (clast-supported to openwork). It exhibits well-defined sub-horizontal stratigraphy and is interpreted as a low -energy channel.

240 The southern third of U50 is itself overlain with a 5-10-cm-thick well-sorted fine sand unit (U40) that changes laterally to massive grey clay with widespread secondary oxidation as it enters a small basin formed by the top of U70 at the southernmost end of the trench. There, U40 displays growth strata and contains massive clay with rare

scattered angular gravels (Fig. 15a). This marks a different depositional environment: a small pond in a rather dry climate with occasional clasts from the surrounding slope.

245 A higher well-developed layer crops out over the whole length of the trench. Unit 30 is composed of massive red clay and coarse sand with abundant scattered gravel and some well-sorted grey sand lenses (Fig. 15a). The clay fraction is dominant within the small depression to the south and diminishes to the north where sand lenses are thicker (5-8 cm) and more continuous. There, the matrix contains a significant fraction of white clay (Fig. 15b). Overall, the stratigraphic facies of U30 resembles red clay formations generally associated with a warm and humid
250 climate (Feng et al., 2007).

Between x = 9 m and x = 12 m, three blocks with well-defined edges make up unit U20 composed of well-stratified sand and angular fine gravel with very little matrix resembling channel fill unit U50. It is considered allochthonous with respect to the rest of the stratigraphic section and interpreted as a small channel that flowed oblique to the fault. A modern equivalent could be seen in the shallow intermittent stream that flows across the site next to trench
255 Muka-K (Fig. 15 b). We collected two samples from the top of U20: W2-S04 yielded an age of 2745 ± 30 BP (calibrated date 945 ± 110 BC) and W2-S05 an age of 1950 ± 30 yr BP (calibrated date 45 ± 80 AD). Since both samples are both bulk sediments the significant age difference may not be attributed to reworking of W2-S04. Furthermore, W2-S05 sits very close to a rupture and exhibits dense live rootlets. Hence, we interpret W2-S05 as contaminated and rejuvenated with respect to its stratigraphic position and discard it from our analysis.

260 Finally, the uppermost unit called U11 is a 0.8-to-1.5-m-thick massive fine sand and silt layer. It is overall grey in color, darker near its base and displays discontinuous brown to black lenses throughout the section. At the southern end of the trench, it contains clasts of U30, which indicates the base of U11 is an erosion surface. Above this local transition, no internal stratigraphy could be observed. Its top is dominated by weak present-day soil development (U10), which is only visible within the first 8-10 cm from the ground surface. We collected two sediment samples
265 from U11 within dark lenses: one at the bottom (sample W4-S02) yielded an age of 2360 ± 30 yr BP (calibrated date 450 ± 70 BC) and one in the mid-section (sample W2-S06) an age of 1180 ± 25 yr BP (calibrated date 860 ± 85 AD). This is the youngest age constraint found in the Muka-L trench.

3.2 Chronology of past surface-rupturing earthquakes

270 Trench Muka-L revealed numerous deformation features (Fig. 15a-e): interrupted and offset layers displaying step-like geometry (Fig. 15a), flower structures (Fig. 15b), and grabens (between 6 m and 7 m in Fig. 15g), among others.

The Carboniferous bedrock (U70) is intensely deformed with widespread fractures and numerous shear zones dipping 30°-50° to the south and containing white to yellow clay. This unit is brittle enough for groundhogs to be
275 able to dig through it (see the large burrow at x = 8 m in Fig. 15f-g). This deformation is inconsistent with ruptures observed in upper units and is limited to U70; it is therefore considered representative of an ancient tectonic regime and will not be described any further here.

The sedimentary section (units U60 to U10) is affected by ruptures exhibiting generally near-vertical dips with some dipping slightly to the south and a few to the north. Flower and double flower structures (Fig. 15 b-e) and 14g at 4.5 m) are the cross-section expressions of horizontal movement along en echelon fissures and indicate a strong strike-slip component. This is confirmed by significant variations in unit thickness across faults as displayed by U60 between 9 m and 12 m. Furthermore, numerous extensional features such as stepping ruptures at the edge of the pond, a graben at 6-6.5 m and the collapse of the whole sedimentary section between 10.5 m and 12 m indicate deformation is transtensional, thus reflecting geomorphological observations. The detailed trench log (Fig. 15 g) reveals that normal geometry ruptures are dominant south of 8 m (main burrow) and expressed as distributed minor vertical individual offsets of 5-15 cm (with a possible contribution from strike-slip displacement). Dominantly strike-slip deformation appears to be limited to a narrow band between 9 m and 12 m. There, large vertical apparent displacements (> 50 cm) and allochthonous blocks suggest significant horizontal deformation.

Logged ruptures display varying terminations. Between 0 m and 3 m and between 5 m and 7.5 m all ruptures terminate at the top of U30 and are truncated by the upper erosion surface. A few more ruptures between 8 m and 9 m appear to display a similar geometry, though extensive burrowing hinders proper observations. These ruptures would have affected the stratigraphy posterior to the deposition of U30 and prior to the erosion of its top surface; i.e. between 1515 ± 90 BC and 945 ± 110 BC. A second generation of ruptures cuts through the whole section and affects U11 and possibly U10 (soil development renders our observations inconclusive): between 3 m and 5 m, at 7 m and between 9 m and 12 m. The event occurred posterior to the deposition of the youngest unit (U11), i.e. since 860 ± 85 AD. It should be noted that a few isolated ruptures located at the edge of the pond (around 3 m) affect the upper erosion surface (top of U30) but do not appear to propagate further upward. Although they could be associated with an intermediate event, we propose they are associated with the most recent one and their upward continuation could not be observed due to the lack of clear stratigraphy within U11. Furthermore, small vertical offsets affect the top of U30 between 3 m and 5 m with an apparent component (the bottom and top of U30 do not display the same offsets).

In summary, the Muka-L trench documents the erosion and deposition record for the last ~3000 yr with varying environments. Abutting relationships reveal at least two deformation events: a penultimate event (PE) at 1605-775 BC and a most recent event (MRE) after 775 AD.

4 Discussion and Conclusions

4.1 Surface trace geometry and Inter-event time

From our morphotectonic analysis based on field observations and HR remote sensing data, we mapped the Sharkhai fault, oriented N57° (±15°), over a length of about 40 km (Fig. 13). The tips of the surface rupture terminate into fluvial plains where they are covered by sediments. Hence, the total surface rupture length of the Sharkhai fault could be underestimated by up to 10 km. The surface expression of the fault is divided into two main segments displaying a slightly arcuate shape and separated by a large extensional step-over of 1.4 km in width. Both segments are of similar length, about 22 km, with a lateral overlap of about 4 km. We also described geometric discontinuities that are typical for large strike slip faults: strike changes of 5° to 9° (from south to north

315   N42°, N50°, N55°, N63° and N72°); local step-overs of 3 m to 173 m in width; secondary branches of 10 m to 1.6
        km in length (mainly at the northern end). Generally, these discontinuities are too small to play an important role
        in the rupture propagation and total length and related earthquake size (Poliakov et al., 2002). The width of the
        main extensional step-over corresponds to features that may equally stop or promote the propagation of the rupture
        in similar settings (Wesnousky, 2006).

320   Along strike, we documented 7 streams affected by left-lateral cumulative offsets ranging from 8 m to 57 m. We
        did not observe systematic vertical deformation; some local vertical displacements being easily explained as
        apparent and induced by horizontal slip along slopes.

        Furthermore, our paleoseimic investigations reveal two paleoearthquakes along the Sharkhai fault: the penultimate
        earthquake (PE) occurred between 1515 ± 90 BC and 945 ± 110 BC and the most recent event (MRE) occurred
325   after 860 ± 85 AD, which yields an inter-event time of 2080 ± 470 yr (between 1610 and 2550 yr). This is the first
        inter-event time constraint for the Sharkhai fault and it is comparable to values derived for major active faults
        elsewhere in Mongolia (e.g. Prentice et al., 2002; Rizza et al., 2015). The Muka trench site is located near the end
        of the mapped rupture (Fig. 4), which is not the standard strategy for such a study since deformation may be weakly
        expressed and the resulting record may be less legible and possibly partial. Potential sites are scarce along the
330   Sharkhai Fault and this site was nevertheless selected on the basis of remote sensing and field observations for its
        relatively high sedimentary potential. It delivered well-expressed surface deformation and adequate deposits for
        age determinations.

4.2 Magnitude, co-seismic displacement and slip rates

335   Finally, we consider four rupture scenarios: i) the entire fault ruptures into a single event over a length of 40 km,
        ii) same as previous with an extended length of 50 km to account for underestimation, iii) the two segments rupture
        independently into two distinct events over lengths of 20 km, and iv) same as previous with extended lengths of
        25 km to account for underestimation (Table 3). Considering the scaling laws proposed by Wells and Coppersmith
        (1994 - named hereafter WC94) and Leonard (2014 - named hereafter L14), we can associate magnitudes and co-
340   seismic slip values to each scenario.

        The deduced magnitudes Mw vary between 6.4 ± 0.2 and 7.1 ± 0.2 and the co-seismic slip values vary between
        0.6 ± 0.5 m and 1.6 ± 1.2 m (table 3). For the scenario when the entire fault breaks in one event, the slip rate is
        between 0.5 ± 0.3 and 0.9 ± 0.5 mm/yr; for the scenario when the two segments break separately, it is between 0.3
        ± 0.3 and 0.4 ± 0.3 mm/yr (Table 4).

345

350   **Table 3:** Estimation of the magnitude and average co-seismic slip using Wells and Coppersmith (1994) and Leonard (2014) regressions. The fault length is determined from the segmentation scenarios.

Segmentation scenario	Rupture length (km)	Magnitude (Mw)		Average co-seismic slip (m)	
		Wells and Coppersmith, 1994	Leonard, 2014	Wells and Coppersmith, 1994	Leonard, 2014
Entire fault	40	6.9 ± 0.2	6.9 ± 0.2	1.3 ± 0.9	1.0 ± 0.4
2 segments	22	6.7 ± 0.2	6.4 ± 0.2	0.6 ± 0.5	0.6 ± 0.4
Entire Fault (observed + 10 km)	50	7.1 ± 0.2	7.0 ± 0.2	1.6 ± 1.2	1.2 ± 0.4
2 segments (observed + 5 km)	27	6.7 ± 0.2	6.5 ± 0.2	0.8 ± 0.6	0.7 ± 0.4

Table 4: Minimum and maximum inter-event time and slip rate for the Sharkhai fault. WC94=Wells and Coppersmith, 1994. L14=Leonard, 2014.

Segmentation scenario	Co-seismic offset (m)	Inter-event time (years) Min / Max	Slip rate (mm/year) Max / Min **average**
Entire fault	1.3 ± 0.9 (WC94) 1.0 ± 0.4 (L14)	1610 / 2550	0.8 ± 0.6 / 0.5 ± 0.3 **0.8 ± 0.6 (WC94)** 0.6 ± 0.2 / 0.4 ± 0.1 **0.5 ± 0.3 (L14)**
2 segments (South and North)	0.6 ± 0.5 (WC94) 0.6 ± 0.4 (L14)	1610 / 2550	0.4 ± 0.2 / 0.2 ± 0.2 **0.3 ± 0.3 (WC94)** 0.4 ± 0.2 / 0.2 ± 0.1 **0.3 ± 0.2 (L14)**
Entire Fault (observed + 10 km)	1.6 ± 1.2 (WC94) 1.2 ± 0.4 (L14)	1610 / 2550	1.0 ± 0.5 / 0.6 ± 0.2 **0.9 ± 0.5 (WC94)** 0.7 ± 0.2 / 0.5 ± 0.1 **0.6 ± 0.3 (L14)**
2 segments (observed + 5 km)	0.8 ± 0.6 (WC94) 0.7 ± 0.4 (L14)	1610 / 2550	0.5 ± 0.2 / 0.3 ± 0.1 **0.4 ± 0.3 (WC94)** 0.4 ± 0.2 / 0.3 ± 0.1 **0.4 ± 0.2 (L14)**

355

The timing of the last event, the inter-event time (1610 - 2550 yr) and the slip rate (less than 1.5 mm/yr) are consistent with the weakly expressed morphology of the fault. Notice that considering the uncertainties, the lowest slip rate value could be as low as ≈ 0.1 mm/yr with the scenario of an event breaking only one segment of the Sharkhai fault every 2550 years. The upper bound (1.5 mm/yr) appears unrealistically high for a single structure

360   in regard to region-wide values and would correspond to the extreme scenario of an event breaking the whole Sharkhai fault + 10 km every 1610 yr.

The first results from a local GPS network deployed in the area since 2010 (Miroshnichenko et al., 2018), show a high heterogeneity in direction and velocities, and local complexities. However preliminary, this is consistent with our observations and previous studies that the region absorbs part of the deformation along various active faults.

365   Several slip rates and recurrence times have been estimated and published in western Mongolia (Calais et al. 2003; Ritz et al., 2006; Etchebes, 2011; Rizza et al., 2015), focused on faults where large earthquakes (M8+) occurred (1905, 1931, 1957) and associated with hundreds of kilometers of surface ruptures (table 5). Their estimated slip rate values, 1.5 to 3.8 mm/yr, are about 2 to 10 times faster than those we estimate on the Sharkhai fault. The recurrence times estimated over there are about twice longer, but the magnitude considered are about 8 and more

370   when it is about 7 for the Sharkhai fault. In western Mongolia, the seismicity (One century of seismicity in Mongolia map, 2000; Dugarmaa and Schlupp, 2000) and slip rates along faults are higher than in the region of Ulaanbaatar. Our results are therefore consistent with other observations in the region. However, our preliminary findings do not favour a specific rupture scenario and associated magnitude for the Sharkhai fault.

375   Table 5: Synthesis of geological or geodesic slip rates and recurrence time for large events published for large faults in western Mongolia.

Fault	Geological slip rate (mm/year)	Recurrence time	Geodesic slip rate (mm/year)
Fu-Yun (EQ M8+ in 1931)	3.8 ± 0.2 (Etchebes, 2011)	3 - 4 ky (Etchebes, 2011)	2.6 ± 0.5 (Calais et al., 2003)
Bolnay (EQ M8+ in 1905)	3.1 ± 1.7 5 (Rizza et al., 2015)	2.43 - 3.1 ky (Rizza, 2010)	2.6 ± 1 (Calais et al., 2003)
Bogd (EQ M8+ in 1957)	1.5 ± 0.26 (Ritz et al., 2006)	3.6 - 3.5 ky (Rizza, 2010)	2 ± 1.2 (Calais et al., 2003)

4.3 Implications for Seismic Hazard Model

By this work, we identified and mapped the Sharkhai active fault that must be included now as an earthquake

380   scenario impacting Ulaanbaatar and its region. As well, it must be included in seismic hazard assessment, upgrading the seismotectonic model, associated to an inter-event time of 2080 ± 470 yr for earthquakes with magnitude Mw between 6.4 and 7.1 ± 0.2, the first estimates on this fault. The both scenarios, with the entire fault breaking in one event and the 2 segments breaking independently, must be considered. If the uncertainties are still substantial, the estimates are consistent with the regional knowledge. This fault is a part of a larger system with

385 several parallel structures, as Hustai and Avdar active faults. The question that arises is if these faults break independently or in a short time sequence followed by a long period of quiescence. For that, complementary studies on these active faults are necessary.

Code/Data availability

390 Not applicable.

Author contribution

AA and all co-authors contributed to all parts of the work and the manuscript.

395 **Competing interests**

The authors declare that they have no conflict of interest

Data and resources

400 Pleiades. High resolution (2m Multispectral, 0.5m Panchromatic) were acquired by Pleiades satellites and broadcast by Astrium.

DEM data: High resolution (12m) topography from DLR's TerraSAR-X / TanDEM-X satellite.

Shuttle Radar Topography Mission 1 Arc-Second Global (DOI: /10.5066/F7PR7TFT), last accessed June 2019.

Google Earth views: http://www.google.com/earth, last accessed July 2017.

405

Acknowledgments

This work was supported in France by the EOST (Ecole et Observatoire des Sciences de la Terre) - IPGS (Institut de Physique de Globe de Strasbourg, now ITES - Institut Terre et Environnement de Strasbourg), University of
410 Strasbourg-CNRS and in Mongolia by IAG (Institute of Astronomy and Geophysics, Academy of Sciences of Mongolia). Access to Pleiades images was supported by CNES (Centre National d'Etudes Spatiales). TanDEM-X data was kindly provided by DLR (Deutsches Zentrum für Luft- und Raumfahrt) through the TanDEM-X Science program (Project DEM_OTHER1719). The authors would like to thank the many colleagues and students from IAG for their help in the field. The authors thank Michel Granet for his support of this work, especially during the
415 PhD work of Abeer Al-Ashkar.

References

Adiya, M. : Seismic activity near Ulaanbaatar: Implication for seismic hazard assessment, Ph.D. thesis, L'Institut Terre et Environnement de Strasbourg (previously: Institut de Physique du Globe de Strasbourg), France, 256
420   pages, 29 September 2016.

Al-Ashkar, A. : Tectonique active de la région d'Oulan Bator, Mongolie : Analyse morpho-tectonique et paléosismologique des failles actives de Sharkhai et Avdar, Ph.D. thesis, L'Institut Terre et Environnement de Strasbourg (previously : Institut de Physique du Globe de Strasbourg), France, 360 pages, 15 Septembre 2015.

Bayasgalan, A.: Active tectonics of Mongolia, Ph.D. Thesis, Trinity College Cambridge, 180p, 1999.

425   Bayasgalan A., Jackson J.A., Ritz J.F., and Cartier S.: Field examples of strike-slip fault terminations in Mongolia and their tectonic significance, Tectonics, 18, 394–411, 1999a.

Bayasgalan, A. and Jackson, J. A.: A re-assessment of the faulting in the 1967 Mogod earthquakes in Mongolia, Geophys. J. Int., 138, 784-800, 1999b.

Biasi G. P., and Wesnousky S. G.: Steps and gaps in ground ruptures: Empirical bounds on rupture propagation,
430   Bull. Seismol. Soc. Am., 96, 1110–1124, 2016.

Biasi, G. P., and Wesnousky, S. G.: Bends and ends of surface ruptures, Bulletin of the Seismological Society of America, 107(6), 2543– 2560, https://doi.org/10.1785/0120160292, 2017.

Calais, E., Vergnolle, M., San'kov, V., Lukhnev, A., Miroshnitchenko, A., Amarjargal, S., and Déverchère, J.: GPS measurements of crustal deformation in the Baikal-Mongolia area (1994–2002): Implications for current
435   kinematics of Asia, J. Geophys. Res., 108, 2501, 2003.

Crone, A. J. and Haler, K. M.: Segmentation and the co-seismic behavior of Basin and Range normal faults: examples from east-central Idaho and southwestern Montana U.S.A., J. Struct. Geol., 13, 151–164, 1991.

440   Cunningham, W.D.: Cenozoic normal faulting and regional doming in the southern Hangay region, Central Mongolia: implications for the origin of the Baikal rift province, Tectonophysics, 331, pp. 389-411, 2001.

Cunningham, W.D.: Structural and topographic characteristics of restraining-bend mountain ranges of Altai, Gobi Altai and easternmost Tien Shan. In: Cunningham W.D., & Mann P. (Eds.), Tectonics of strike-slip restraining
445   and releasing bends, Geol. Soc., London, Special Publications, pp. 219–237, 2007.

Cunningham, W.D., Windley, B.F., Dorjnamjaa, D., Badamgarov, G., and Saandar, M.: A structural transect across the Mongolian Altai: Active transpressional mountain building in central Asia, Tectonics, 15, 142-156,1996.

De Polo, C. M., Clark, D.G., Slemmons, D.B. and Rameli, A. R.: Historical surface faulting in the Basin and Range province, western North America-implication for fault segmentation, Journal of Structural Geology, 13, 1991.

450   Dorjpalam, S., Kawase, H., Ho, N.: Earthquake Disaster Simulation for Ulaanbaatar, Mongolia Based on The Field Survey and Numerical Modeling of Masonry Buildings, 13th World Conference on Earthquake Engineering Vancouver, B.C., Canada, pp. 461, 2004.

Dugarmaa, T. and Schlupp, A.: One century of seismicity in Mongolia map (1900–2000), in: Proc. MAS 4, No. 170, pp. 7–14, 2000.

455   Dujardin, J.R, Bano, M., Schlupp, A., Ferry, M., Ulziibat, M., Tsend-Ayush, N., and Enkhee B.: GPR measurements to assess the Emeelt active fault's characteristics in a highly smooth topographic context, Mongolia, Geophys. J. Int, https://doi.org/10.1093/gji/ggu130, 2014.

Etchebes, M. : Paléosismologie spatiale : segmentation et scénarios de ruptures sismiques La faille de Fuyun et la faille du Kunlun, Chine, Ph.D. thesis, Institut de Physique du Globe de Paris (IPGP), France, 400pp, 2011.

460   Finzi, Y. and Langer, S.: Damage in stop-overs may enable large cascading earthquakes, Geophysical Research Letters, 39: L16303. DOI: 10.1029/2012GL052436, 2012.

Feng, Z. D., Zhai, X. W., Ma, Y. Z., Huang, C. Q., Wang, W. G., Zhang, H. C. et al. : Eolian environmental changes in the Northern Mongolian Plateau during the past ~ 35,000 yr, Palaeogeography, Palaeoclimatology, Palaeoecology 245(3-4): 505-517, 2007.

465   Ferry, M., Schlupp, A., Munkhuur, U., Munschy, M., Fleury, S., Baatarsuren G., Erdenezula, D., Munkhsaikhan, A., and Ankhtsetseg, D.: Tectonic Morphology of the Hustai Fault (Northern Mongolia), A Source of Seismic Hazard for the city of Ulaanbaatar, EGU General Assembly, Vienna, Austria, 2010.

Ferry, M., Schlupp, A., Munkhuur, U., Munschy, M., and Fleury, S.: Tectonic morphology of the Hustai Fault (Northern Mongolia), EGU General Assembly, Vienna, Austria, 2012.

470   Fleury, S., Munschy, M., Schlupp, A., Ferry, M., Bano, M., and Munkhuu, U.: High-resolution magnetic survey to study Hustai Fault (northern Mongolia), AGU Fall Meeting, San Francisco, California, USA, 2011.

Fleury, S., Munschy, M., Schlupp, A., Ferry, M., and Munkhuu, U.: High resolution magnetic survey across the Emeelt and Hustai faults near Ulaanbaatar, Mongolia, EGU General Assembly, Vienna, Austria, 2012.

Harris, R. A., Archuleta, R. J. and Day, M.: Fault steps and the dynamic rupture process: 2-D digital simulations
475   of a spontaneously propagating shear fracture, Geophys. J. Int.,18, 893–896,1991.

Imaev, V.S., Smekalin, O.P., Strom, A.L., Chipizubov, A.V., and Syas'ko, A.A.: Seismic-hazard assessment for Ulaanbaatar (Mongolia) on the basis of seismogeological studies, Russian Geology and Geophysics, 53, 9, 906-915, 2012.

480   Khilko, S.D., Kurushin, R.A., Kochetkov, V.M., Misharina, L.A., Melnikova, V.I., Gilyova, N.A., Lastochkin, S.V., Baljinnyam, I., and Monhoo D.: Earthquakes and the base of the seismic zoning of Mongolia, The joint Soviet-Mongolian scientific - Research Geological Expedition, 41, 225 pages, 1985.

Klinger Y.: Relation between continental strike-slip earthquake segmentation and thickness of the crust, J. Geophys. Res, 115: B07306. DOI: 10.1029/2009jb006550, 2010.

Leonard, M.: Self-consistent earthquake fault scaling relations: Update and extension to stable continental strike
485   slip faults, Bull. Seismol. Soc. Am., 104(6), 2953–2965, 2014.

Lettis, W., Bachhuber, J., Witter, R., Brankman, C., Randolph, C. E., Barka, A., Page, W. D., and Kaya, A.: Influence of Releasing Step-Overs on Surface Fault Rupture and Fault Segmentation: Examples from the 17 August 1999 Izmit earthquake on the North Anatolian Fault, Turkey, Bull. Seismol. Soc. Am., 92, 19–42, 2002.

Manandhar, S., Hino, T., and Kitag, K.: Influences of Long-Term Tectonic and Geo-Climatic Effects on
490   Geotechnical Problems of Soft Ground - Ulaanbaatar, Mongolia, Lowland Technology International, 18(1): 51-58 International Association of Lowland Technology (IALT): ISSN 1344-9656, 2016.

Miroshnichenko, A.I., Radziminovich, N.A., Lukhnev, A.V., Zuev, F.L., Demberel, S., Erdenezul, D., and Ulziibat, M.: First results of GPS measurements on the Ulaanbaatar geodynamic testing area, Russian Geology and Geophysics 59, 1049–1059, 2018.

495   Nuramkhaan, B., Nakane, Y., Yamasaki, S., Otgonbaatar, J., Nuramkhaan, M., Takeuchi, M., Tsukada, K., Katsurada, Y., Gonchigdorj, S., and Sodnom, K.: Description of a NW trending brittle shear zone, Ulaanbaatar, Mongolia. Bull, Nagoya Univ. Museum, No. 28, 39–43, 2012.

One century of seismicity in Mongolia map (1900 - 2000): Coordinators: Dr. Dugarmaa, T., and Dr. Schlupp, A. ; Authors: Adiya M., Ankhtsetseg D., Baasanbat Ts., Bayar, G., Bayarsaikhan, Ch., Erdenezul, D., Möngönsüren,
500   D., Mönkhsaikhan, A., Mönkhöö, D., Narantsetseg, R., Odonbaatar, Ch., Selenge, L., Dr. Tsembel, B., Ölziibat, M., Urtnasan, Kh. and in collaboration with DASE and (RCAG)

Odonbaatar Chimed: Site effects characterization in the basin of Ulaanbaatar, Ph.D. thesis, Université de Strasbourg- France, 184p., https://tel.archives-ouvertes.fr/tel-00785708, 2011.

Parfeevets, A.V. and Sankov, V.A. : Late Cenozoic tectonic stress fields of the Mongolian microplate Champs de
505   contraintes tectoniques fini-cénozoïques dans la microplaque de Mongolie, Comptes Rendus Géoscience, Volume 344, Issues 3–4, Pages 227-238, 2012.

Poliakov, A. N. B., Dmowska, R., and Rice, J. R.: Dynamic shear rupture interactions with fault bends and off-axis secondary faulting, J. Geophys. Res. 107(B11), 2295, doi:10.1029/2001JB000572, 2002.

Ramsey, B.C. and Lee, S.: Recent and Planned Developments of the Program OxCal. Radiocarbon , Volume 55,
510   Issue 2: Proceedings of the 21st International Radiocarbon Conference (Part 1 of 2), pp.720–730, DOI: https://doi.org/10.1017/S0033822200057878, 2013.

Reimer, P.: IntCal13 and Marine13 Radiocarbon Age Calibration Curves 0–50,000 Years calBP, Radiocarbon, 55, 1869–1887, 2013.

Ritz, J.-F., Bourle 's, D., Brown, E.T., Carretier, S., Chery, J., Enhtuvshin, B., Galsan, P., Finkel, R.C., Hanks,
515   T.C., Kendrick, K.J., Philip, H., Raisbeck, G., Schlupp, A., Schwartz, D.P., Yiou, F.: Late Pleistocene to Holocene slip rates for the Gurvan Bulag thrust fault (Gobi-Altay, Mongolia) estimated with 10Be dates, J. Geophys. Res., 108 (B3), p. 2162, 2003.

Ritz, J. F., Braucher, R., Brouw, E. T., Carretier, S., and Bourlès, D. L.: Using in situ-produced 10Be to quantify active tectonics in the Gurvan Bogd mountain range (Gobi-Altay, Mongolia), Geological., 415, 87–110, 2006.

520   Rizza, M. : Analyses des vitesses et des déplacements co-sismiques sur des failles décrochantes en Mongolie et en Iran, Ph.D. thesis, université Montpellier II, France, 408 pages, 5 décembre 2010.

Rizza, M., Ritz, J.-F., Braucher, R., Vassallo, R., Prentice, C., Mahan, S., McGill, S., Chauvet, A., Marco, S., Todbileg, M., Demberel, S., Bourlès D.: Slip rate and slip magnitudes of past earthquakes along the Bogd left-lateral strike-slip fault (Mongolia), Geophys. J. Int., 186, 897–927, 2011.

525   Rizza, M., Ritz, J.-F., Prentice, C., Vassallo, R., Braucher, R., Larroque, C., Arzhannikova, A., Arzhannikov, S., Mahan, S., Massault, M., Michelot, J.-L., Todbileg, M., and ASTER Team: Earthquake Geology of the Bulnay Fault (Mongolia). Bull. Geol. Soc. Am., 105, 2015.

Schlupp, A. : Néotectonique de la Mongolie Occidentale analysée à partir de données de terrain, sismologiques et satellitaires, Ph.D. Thesis, Louis Pasteur university, Strasbourg, France, 256pp, 1996.

530   Schlupp, A., Ferry M., Munkhuu, U., Munschy, M., Fleury, S., Adiya, M., Bano, M., and Baatarsuren, G.: The Emeelt active fault, revealed by the outbreak of micro seismicity, and its impact on the PSHA of Ulaanbaatar, capital of Mongolia, Part I: seismotectonic analysis, ESC General Assembly, Montpellier, France, 2010a.

Schlupp, A., Ferry, M., Munkhuu, U., Munschy, M., and Fleury, S.: Tectonic Morphology of the Hustai Fault (Northern Mongolia): Implications for Regional Geodynamics, AGU Fall Meeting, San Francisco, USA, 2010b.

535   Schlupp, A., Ferry, M., Ulziibat, M., Baatarsuren, G., Munkhsaikhan, A., Bano, M., Dujardin, J-M., Nyambayar, Ts., Sarantsetseg, L., Munschy, M., Fleury, S., Mungunshagai, M., Tserendug, Sh., Nasan-Ochi,r T., Erdenezul, D., Bayarsaikhan, E., batsaikhan, Ts., and Demberel, S.: Investigation of active faults near Ulaanbaatar, Implication for seismic hazard assessment, ASC General Assembly of Asian Seismological Commission, Ulaanbaatar, Mongolia, 2012.

540   Takeuchi, M., Tsukada, K., Suzuki, T., Nakane, Y., Sersmaa, G., Manchuk, N., Kondo, T., Matsuzawa, N., Bacht, N., Khishigsuren, S., Onon, G., Katsurada, Y., Hashimoto, M., Yamasaki, S., Matsumoto, A., Oyu-Erdene, B., Bulgantsetseg, M., Kundyz, S., Enkhchimeg, L., Ganzorig, R., Myagmarsuren, G., Jamiyandagva, O., and Molomjamts, M.: Stratigraphy and geological structure of the Palaeozoic system around Ulaanbaatar, Mongolia, Bulletin of the Nagoya University Museum, No.28, 1-18, 2013.

545   Tomurtogoo, O., Byamba, J., Badarch, G., Minjin, Ch., Orolmaa, D., Khosbayar, P., and Chuluun, D.: Geologic
       map of Mongolia. Scale 1:1000000. Mineral Resources Authority of Mongolia, Ulaanbaatar, 1998.

       Tumurbaatar, Z., Miura, H., Tsamba, T.: Site Effect Assessment in Ulaanbaatar, Mongolia through Inversion
       Analysis of Microtremor H/V Spectral Ratios, Geosciences, 9, 228; doi: 10.3390/geosciences, 9050228, 2019.

       Walker, R.T., Molor, E., Fox, M., Bayasgalan, A.: Active tectonics of an apparently aseismic region: distributed
550   active strike-slip faulting in the Hangay Mountains of central Mongolia, Geophys. J. Int., 174, pp. 1121-1137,
       2008.

       Wells, D. L. and Coppersmith, K. J.: New Empirical Relationships among Magnitude, Rupture Length, Rupture
       Width, Rupture Area, and Surface Displacement, Bull. Seismol. Soc. Am., 84, 974–1002, 1994.

       Wesnousky Steven G.: Predicting the endpoints of earthquake ruptures, Nature. 444, 358-360. DOI:
555   10.1038/nature05275, 2006.
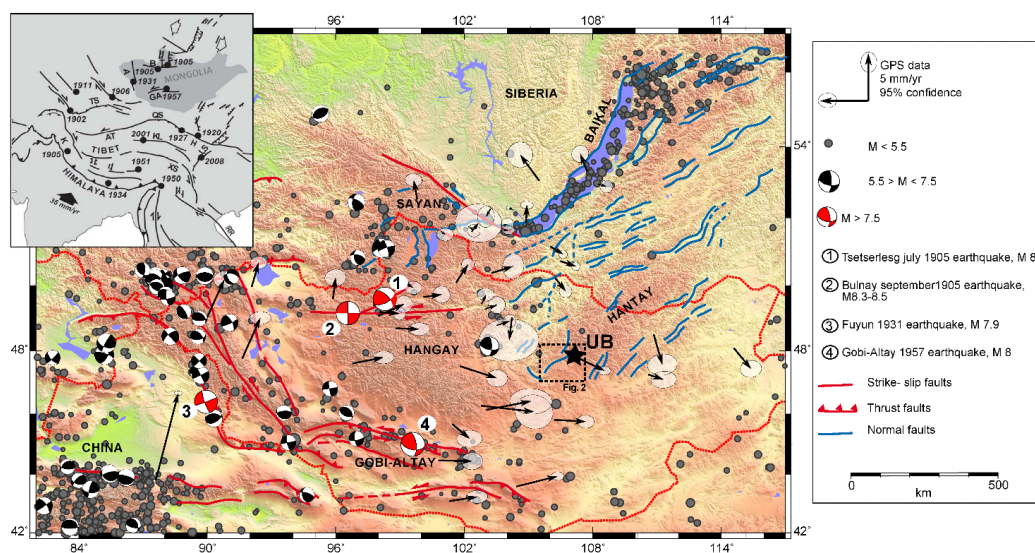
560   **Figure 1**: Tectonic map of Mongolia showing the major active faults and seismic activity with centroid moment tensor solutions
       (adapted from Rizza et al., 2015). Gray dots are the epicenter of earthquakes that happened between 1980 and 2008. Not the
       four great earthquakes of magnitude 8+ (labeled 1 to 4) that occurred since 1905. The inset map shows active deformations in
       Asia. Note the position of Mongolia between the India-Asia collision at the south and extensive structures of the Baikal Rift
       at the north. The black circle shows the major earthquakes (M ≧ 8). The rectangle shows the area in Fig. 2.

565
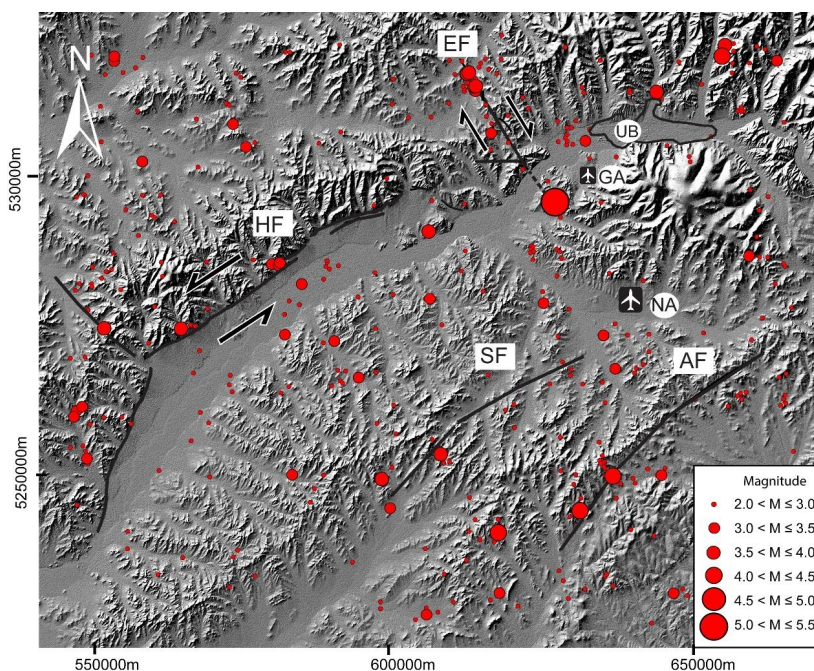
Figure 2: Seismic activity observed in the area of Ulaanbaatar between 1994 and 2011 from the IAG-MAS NDC (Institute of
570   Astronomy and Geophysics, Mongolian Academy of Sciences, National Data Center). The black lines represent the active
faults. HF: Hustai fault, EF: Emeelt fault, SF: Sharkhai fault, AF: Avdar fault, UB: Ulaanbaatar, GA: Ghingis Khan old
international airport, NA = new international airport. Seismic swarms are concentrated along the Emeelt fault. The background
DEM is from SRTM1 data (see data and resources).

575
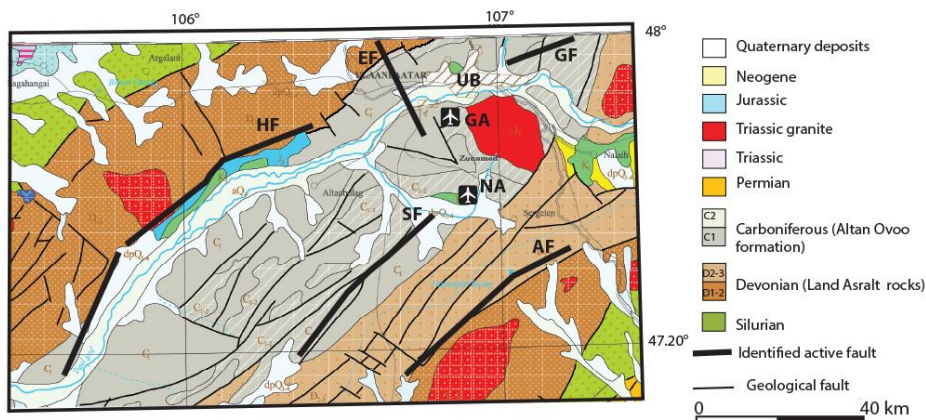
Figure 3: Geological map of the area of Ulaanbaatar and surroundings modified from Geologic map of Mongolia. Scale 1.000000 (Tomurtogoo et al, 1998). GF: Gunj fault, EF: Emeelt fault, HF: Hustai fault and SF: Sharkhai fault AF: Avdar fault. The AF, SF, and HF are in a large post carboniferous synclinal. Note the urban region of Ulaanbaatar (UB), the old (GA) and new international airport (NA).
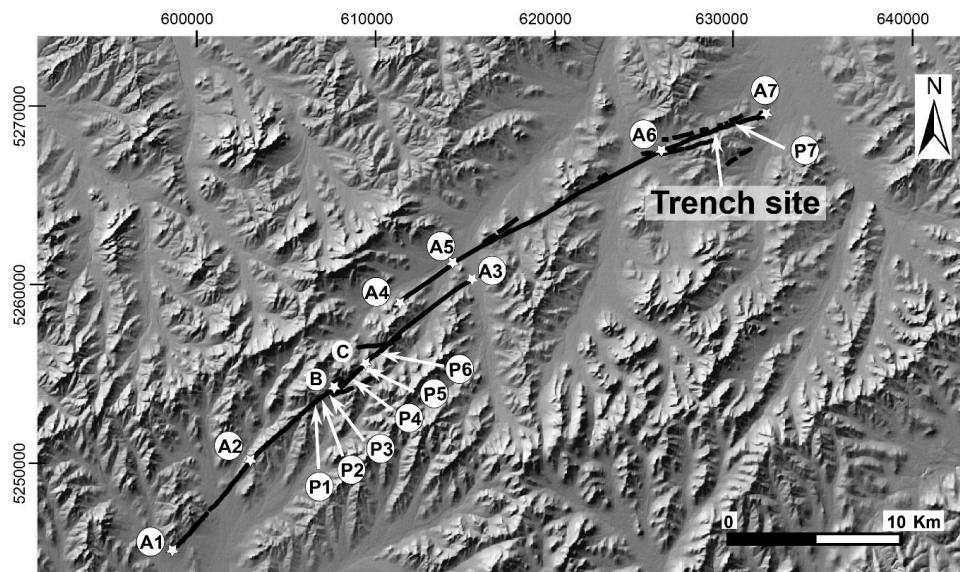
580

Figure 4: The Sharkhai fault identified at surface is about 46 km long and strikes between 42° and 72° NE. Letters (A1-A7, B and C) and stars indicate the coordinate points in the text. P1, P2, P3, P4, P5, P6 and P7 are shifted drainages locations. Note the left step-over which divides the fault in two sections, south and north sections. The background DEM is from SRTM1 data, coordinates are UTM 48N (see data and resources).

585
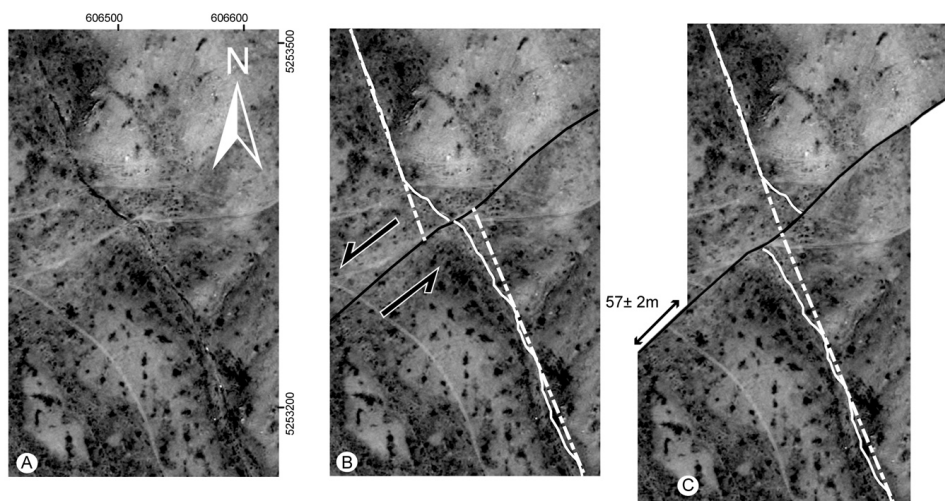
Figure 5: Drainage P1 shifted by 57 ± 2 m of cumulative left-lateral movement. A) Present-day situation: Panchromatic Pleiades image displaying the shifted drainage. B) Present-day situation with drainage and fault: the offset is measured on images by projecting the average upstream and the downstream to the fault trace. C) Reconstruction of the drainage to its initial

590   position after back slip along the fault. The uncertainty of the offset is estimated by realizing several reconstruction tests. The water flow direction is to the south. For location, see Fig. 4.
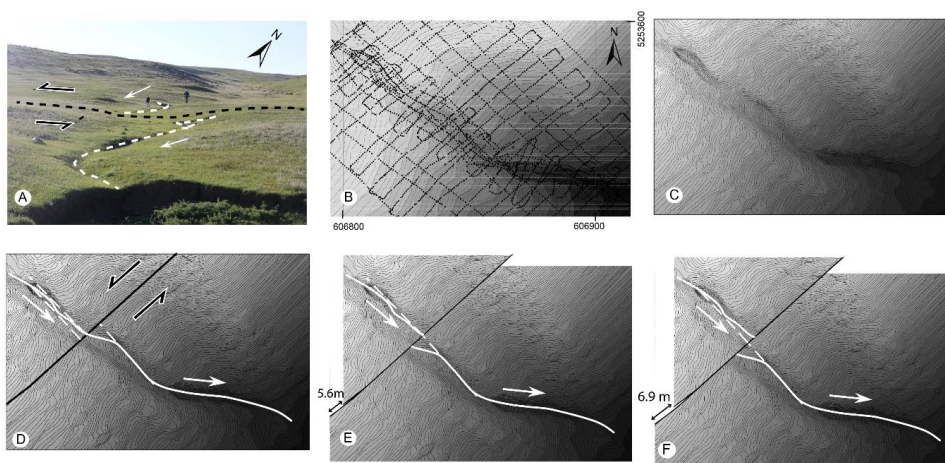
Figure 6: Offset of drainage P2. A) Photograph of P2: black line indicates the fault trace. The north direction in the photograph

595   is approximate. B) Differential GPS measurements used to build the digital topographic map. C) Digital topographic map. D) Present-day situation: the offset is measured on images by projecting the average upstream and the downstream to the fault trace. We consider for the upstream a "wide zone" giving an uncertainty on its piercing position for the back-slip reconstruction. E) If we consider the minimum back slip, we measure 5.6 m and F) if we consider the maximum back slip, we measure 6.9 m. Hens the left-lateral offset is estimated at 6.25 ± 0.65 m. White arrows: water flow direction. For location, see Fig. 4.

600
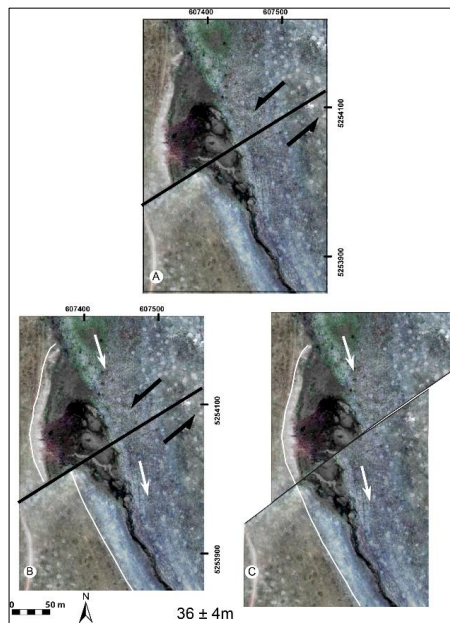
Figure 7: Quaternary deposits (P3), formed by drainages, affected by left lateral offset. A) © Google earth image (see data and resources) showing the various Quaternary deposits (changes in color) overlapped with the location of the surface rupture. B)
605   Panchromatic Pleiades image. C) Present-day situation. The fault traces are marked with black lines. The NE side of the deposits is hidden. D) Reconstruction of the side SW of the deposit to its initial situation shows a 36 ± 4 m of cumulative left lateral offset (White arrows indicate drainage direction). For location, see Fig. 4.
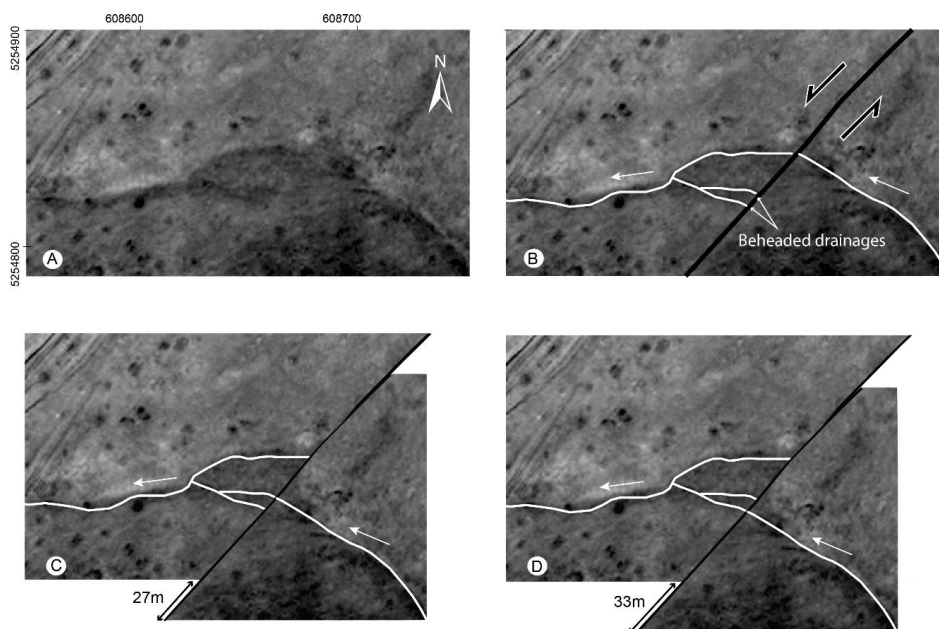
Figure 8: Offset of drainage P4. A) Panchromatic image. B) Present-day situation overlapped with the left lateral shifted drainage and the fault. To match the corresponding piercing points C) the minimum back slip gives 27 m and D) the maximum back slip gives 33 m. Hens the left-lateral offset is estimated at 30 ±3 m. For location see Fig. 4.
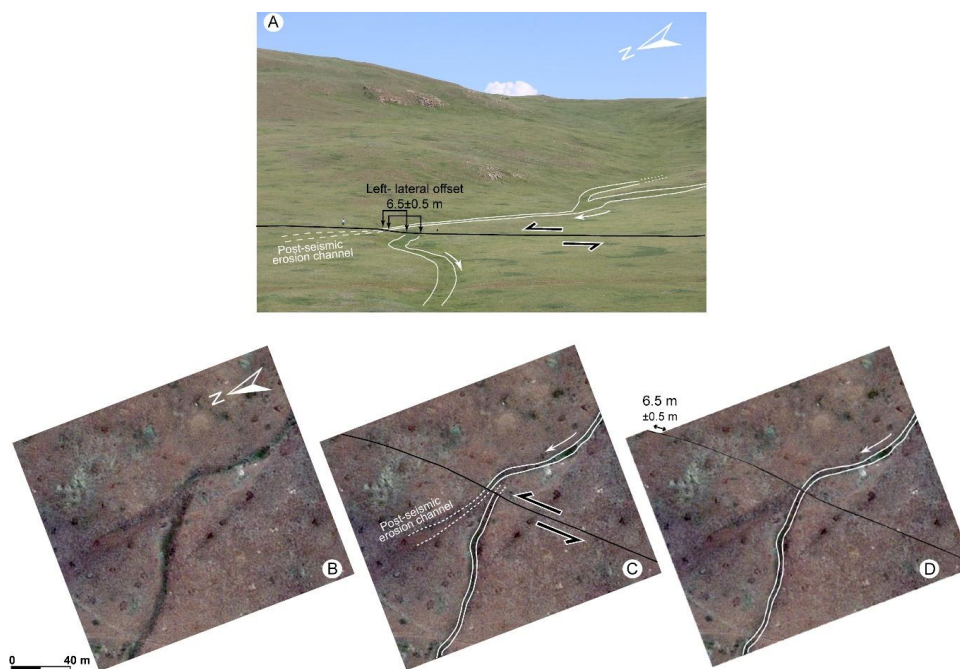
Figure 9: Offset of drainage P5 on the Sharkhai fault. A) Photograph of shifted drainage: black line indicates the fault trace. The north direction in the photograph is approximate. B) Panchromatic image of P5. C) Present-day situation overlapped with the fault (black) and the paleo river disconnected when crossing the fault. Note the post-seismic erosion due to the upstream flow that crosses the fault. D) Reconstruction of the drainage to its initial situation yields 6.5 ± 0.5 m of cumulative left-lateral offset. The uncertainty associated with the offset estimation is obtained by realizing several retro-deformations. For location see Fig. 4.

630
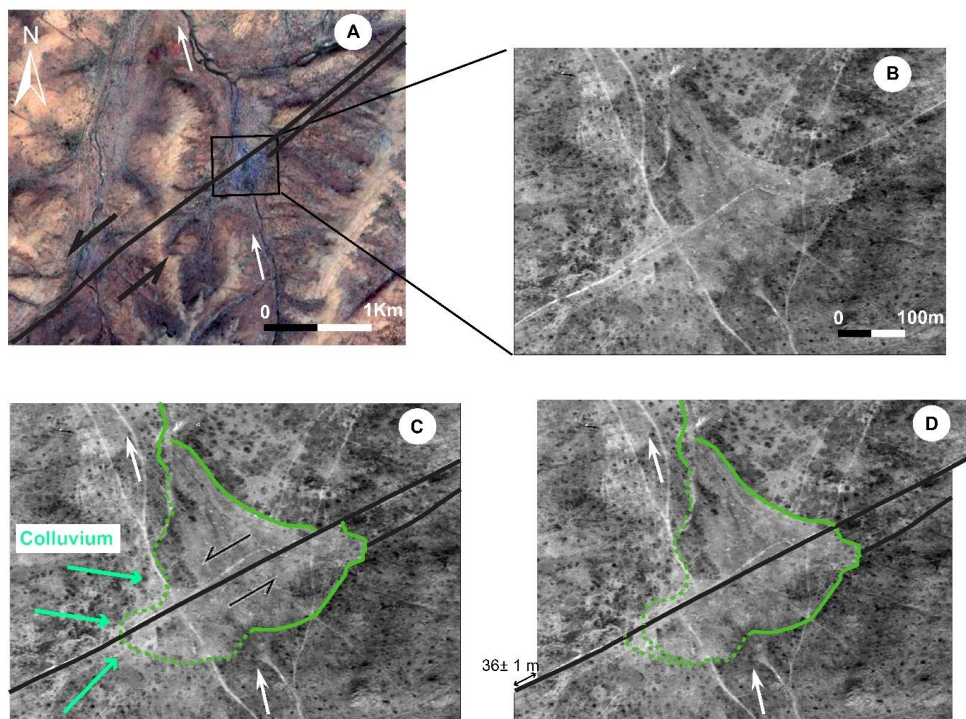
Figure 10: Left-lateral offset affecting Quaternary deposits (P6 at 609957.1 m E , 5256060.72 m N). A) © Google earth imagery (see data and sources) overlapped with the surface rupture and the location of the images B to D. B) Panchromatic image. C) Present-day situation. Panchromatic image overlapped with the fault traces marked with black lines and Quaternary deposits

635 trapped (green limits). The SW side of the trapped Quaternary deposits has been covered by lateral colluvions from NW hill (light green arrows) hiding the real limit of Quaternary trapped deposits (dashed green line). D) Reconstruction of the NE side of the Quaternary trapped deposit to its initial situation shows a 36 ±1 m of cumulative left lateral offset (White arrows indicate drainage direction). For location see Fig. 4.

640
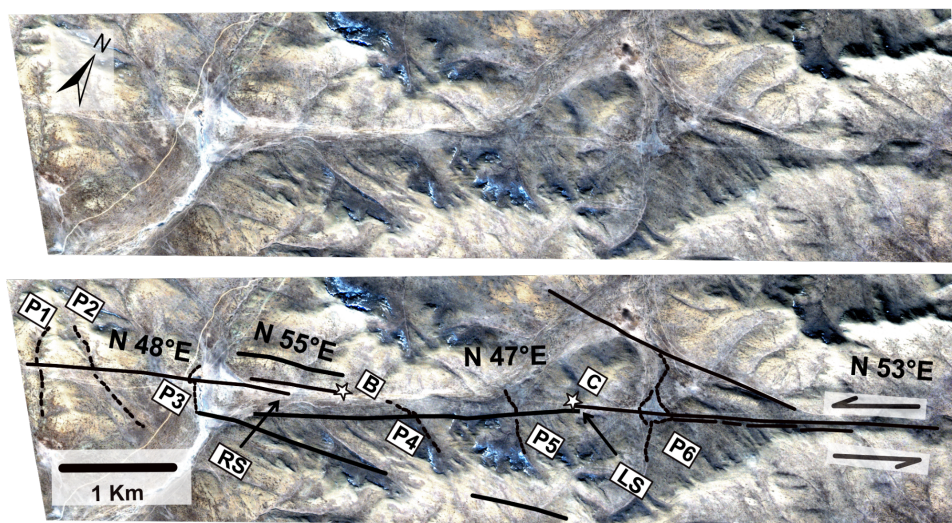
Figure 11 : Mapping of the fault (black line) covering the central part of the southern segment. P1, P2, P3, P4, P5 and P6 are shifted drainages. Left step-over (LS) and right step-over (RS) are of 173 m and 61 m width respectively. The strike changes locally from N47° to N55°. Several secondary branches of lengths between 190 m and 1.6 km are either parallel or oblique to the main rupture. In background, Pleiades satellites images (multispectral RGB-NIR) with 2 m resolution. See text for details and Fig. 4 for location.
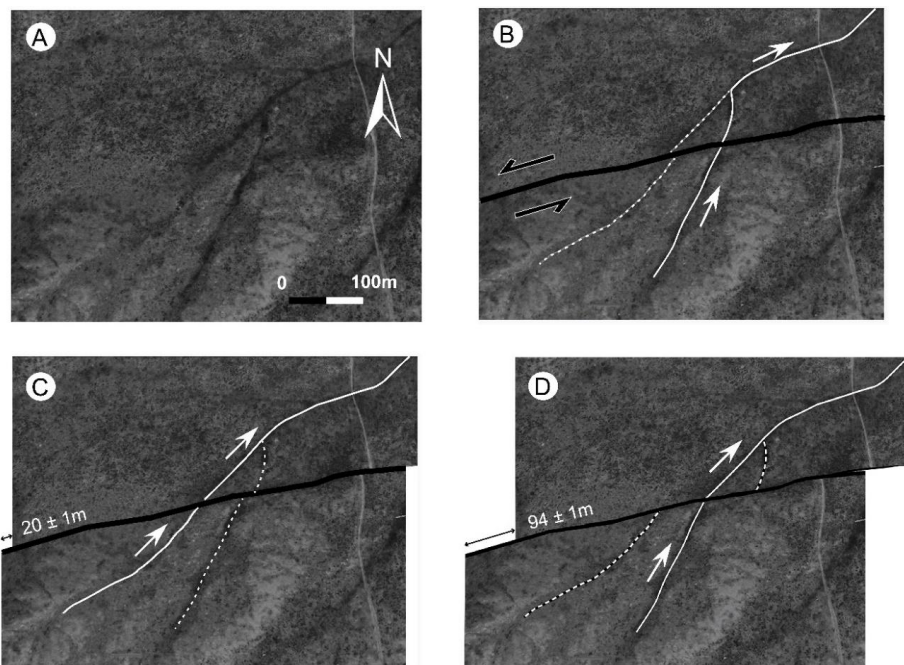
650

Figure 12: Left-lateral shifted stream of (P7 at 630.500 m E and 5.269.000 m N UTM). A) © Google Earth image (see data and sources) showing the present situation. B) Image A overlapped with the fault trace (black) and the shifted drainage (white). Reconstruction of the drainage to its initial situation gives a minimum back slip of 20 ±1 m (C), and the maximum back slip gives 94 ±1 m (D). Hens the left-lateral offset is estimated at 57 ±1 m. For location see Fig. 4.
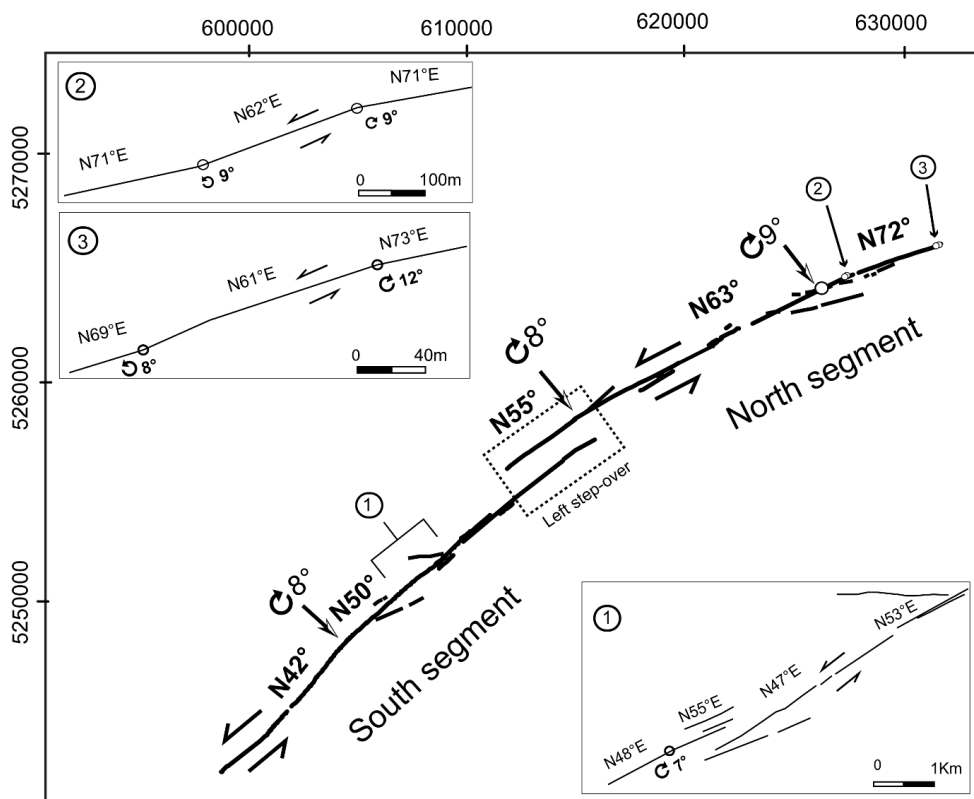
655

Figure 13: Map of surface ruptures and major strike changes (according to the average direction of every segment) and places of interest along the Sharkhai fault. Note the left step-over (dashed rectangle) which divides the fault in two main segments, south and north segments with a local 5° clockwise strike change (from 50° N to 55° N). The average strike change between the south and north segments is larger, with 13° clockwise (50° N to 63° N). Inserts 1, 2, and 3: Zoom on local strike changes
660   along the main rupture (for location along the fault, see rectangle with figure number in circle).
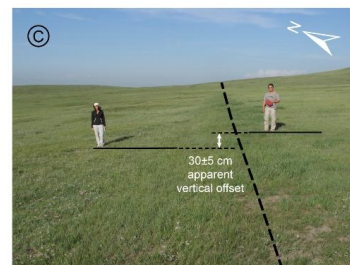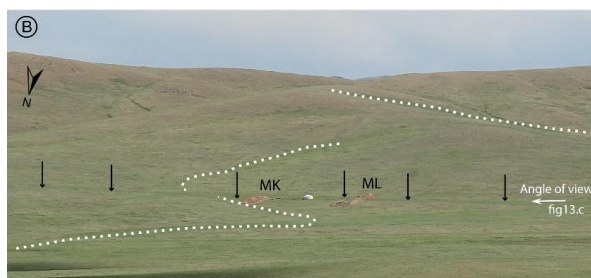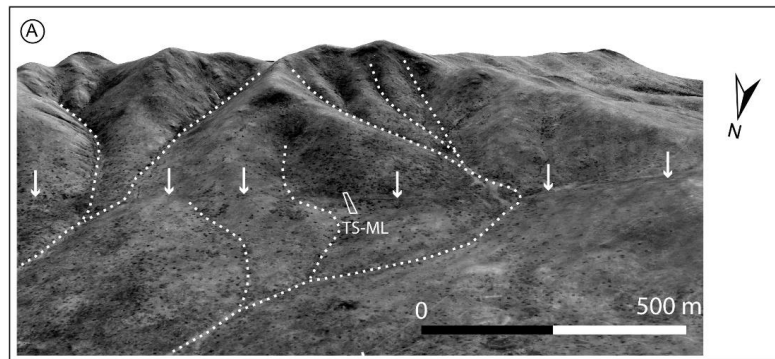
Figure 14: A) High resolution DEM (TanDemX data at 12 m resolution, see Data and Resources) shows the trench site (TS-ML), the fault (white arrows) and the temporary drainages (dashed white lines). B) Location of the trench site (ML and MK excavations) on the north segment of the Sharkhai fault. C) Field photograph taken from the west to the east along the fault, before excavation, shows the fault trace marked by a vegetation contrast (Dashed line). We can note the small component of apparent vertical movement (about 30 ± 5 cm). For location see Fig. 4.
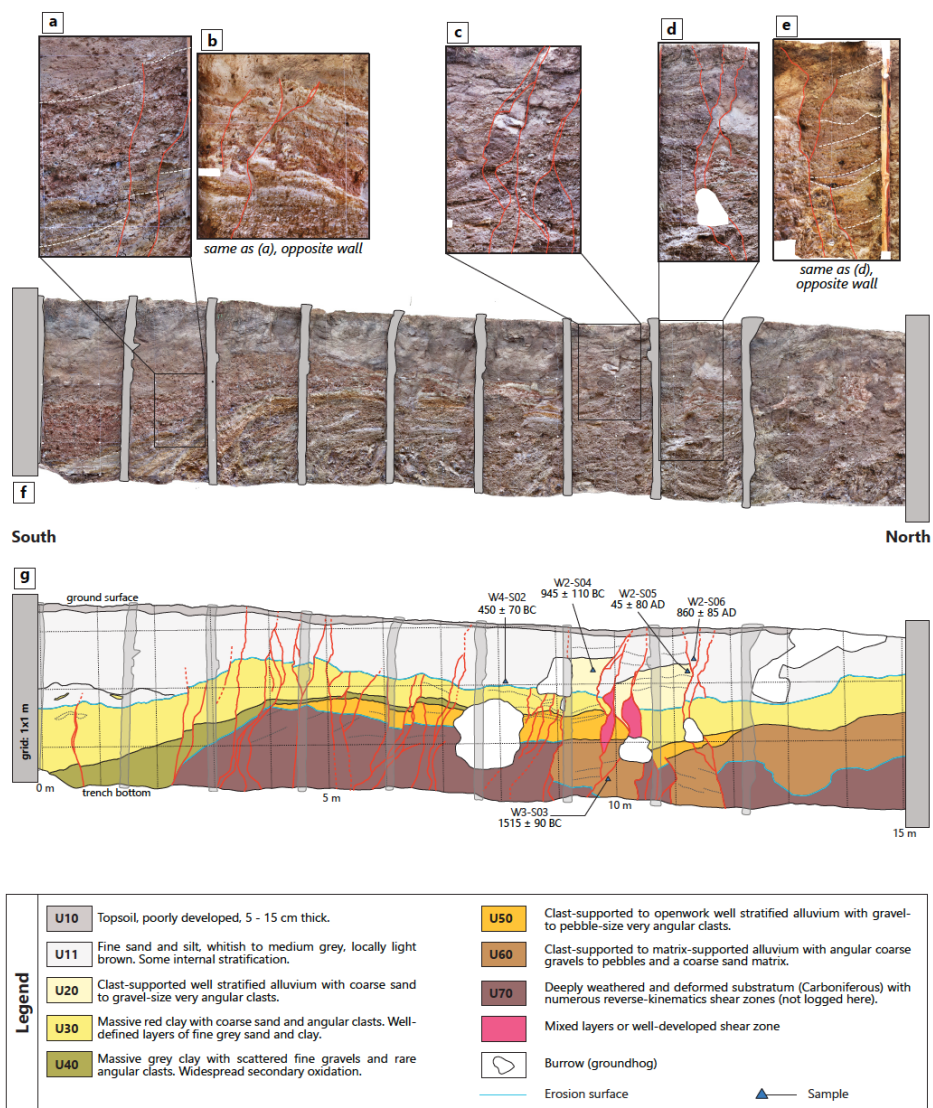
Figure 15: Muka-L trench exposure. a) to e): Close-ups showing deformation features (step-like geometry, flower structures, apparent offsets). f) General orthophotomosaic of the west wall, originally rendered at 1 mm resolution. g) Detailed paleoseismic log of the west wall. The ruptures associated with the last two events are in red. See text for details.